LETTER TO THE EDITOR

The far-infrared/submillimeter properties of galaxies located behind the Bullet cluster [⋆]

M. Rex[1], T. D. Rawle[1], E. Egami[1], P. G. Pérez-González[2,1], M. Zemcov[3,4], I. Aretxaga[5], S. M. Chung[6], D. Fadda[7], A. H. Gonzalez[6], D. H. Hughes[5], C. Horellou[8], D. Johansson[8], J.-P. Kneib[9], J. Richard[10], B. Altieri[11], A. K. Fiedler[1], M. J. Pereira[1], G. H. Rieke[1], I. Smail[10], I. Valtchanov[11], A. W. Blain[3], J. J. Bock[3,4], F. Boone[12,13], C. R. Bridge[3], B. Clement[9], F. Combes[13], C. D. Dowell[3,4], M. Dessauges-Zavadsky[14], O. Ilbert[9], R. J. Ivison[15,16], M. Jauzac[9], D. Lutz[17], A. Omont[18], R. Pelló[12], G. Rodighiero[19], D. Schaerer[14,12], G. P. Smith[20], G. L. Walth[1], P. van der Werf[21], M. W. Werner[4], J. E. Austermann[22], H. Ezawa[23], R. Kawabe[23], K. Kohno[24,25], T. A. Perera[26], K. S. Scott[27], G. W. Wilson[28], and M. S. Yun[28]

(Affiliations can be found after the references)

Received March 31, 2010; accepted May 18, 2010

ABSTRACT

The *Herschel* Lensing Survey (HLS) takes advantage of gravitational lensing by massive galaxy clusters to sample a population of high-redshift galaxies which are too faint to be detected above the confusion limit of current far-infrared/submillimeter telescopes. Measurements from 100–500 μm bracket the peaks of the far-infrared spectral energy distributions of these galaxies, characterizing their infrared luminosities and star formation rates. We introduce initial results from our science demonstration phase observations, directed toward the Bullet cluster (1E0657-56). By combining our observations with LABOCA 870 μm and AzTEC 1.1 mm data we fully constrain the spectral energy distributions of 19 MIPS 24 μm-selected galaxies which are located behind the cluster. We find that their colors are best fit using templates based on local galaxies with systematically lower infrared luminosities.This suggests that our sources are not like local ultra-luminous infrared galaxies in which vigorous star formation is contained in a compact highly dust-obscured region. Instead, they appear to be scaled up versions of lower luminosity local galaxies with star formation occurring on larger physical scales.

Key words. Infrared: galaxies – Submillimeter: galaxies – Galaxies: evolution – Galaxies: high-redshift – Galaxies: clusters: general – Gravitational lensing:strong

1. Introduction

Luminous (and ultra-luminous) infrared galaxies ((U)LIRGS) are a population of massive star-forming galaxies which contain significant amounts of dust, absorbing the ultraviolet emission from newly formed stars within them and re-radiating this energy at far-infrared (FIR) wavelengths. The FIR emission of these sources is therefore strongly correlated with their level of star formation activity (e.g. Kennicutt 1998). *Spitzer* MIPS measurements from 24–160 μm bracket the peak of the dust emission from nearby (U)LIRGS. Therefore, MIPS observations have been very successful in characterizing the spectral energy distributions (SEDs) and star formation rates (SFRs) of the local population (e.g. Rieke et al. 2009). Similar measurements at FIR/submillimeter (submm) wavelengths are required to constrain the SEDs of their higher redshift counterparts. Together the PACS (Poglitsch et al. 2010) and SPIRE (Griffin et al. 2010) instruments on-board *Herschel* (Pilbratt et al. 2010) provide sensitive measurements of this population at five wavelengths from

100–500 μm, sampling the rest-frame peak of the FIR emission out to a redshift of $z = 4$.

The depth of submm maps is ultimately limited by confusion noise resulting from a high density of sources relative to the angular resolution of the telescope. Gravitational lensing by massive galaxy clusters provides the only means to sample an abundant population of intrinsically faint or high-redshift infrared (IR) galaxies which lie below this limit. The *Herschel* Lensing Survey (HLS) (Egami et al. 2010) will target ∼ 40 galaxy clusters with PACS and SPIRE to compile the first significant submm catalog of these galaxies. In this letter we present initial results from our science demonstration phase observations: 8 ′× 8′ PACS maps and 17 ′× 17′ SPIRE maps centered on the Bullet cluster (1E0657-56). Details of these observations are presented in Egami et al. (2010). This is a unique target because of its strong lensing potential and the richness of existing ancillary data. We present the FIR properties of 19 MIPS 24 μm-selected galaxies which are located behind the Bullet cluster. We compare the shapes of their SEDs with those of local (U)LIRGS, and compare their measured IR luminosities with predictions which extrapolate this quantity from the observed MIPS 24 μm flux. Subsequent uses of MIPS in the text refer to the MIPS 24 μm band.
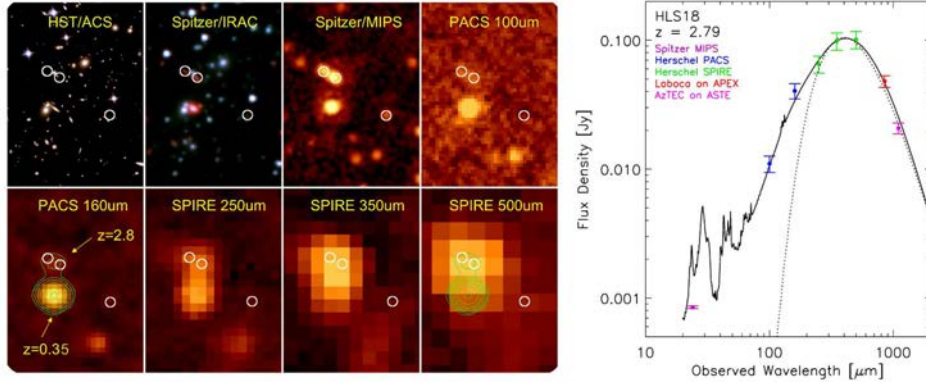
Fig. 1. The most highly magnified galaxy in our sample, HLS18, is the same LIRG first detected by Wilson et al. (2008) with AzTEC at 1.1 mm. *Left panel*: 1.5′×2′ thumbnails of the source at a variety of wavelengths highlight the importance of multi-wavelength data to guide the interpretation of the lower resolution maps. IRAC data reveal three lensed images of the galaxy indicated with white circles, although only emission from the two brightest images is detected in the *Herschel* maps. *Right panel*: Rieke et al. (2009) SED template fit to the source. The fluxes include the contribution from both of the brightest images of the galaxy, indicated by the two left-most circles in the thumbnails. The data points have not been de-magnified. The 24 μm flux is plotted for reference, although it was not used in the fit. The best-fit modified blackbody is shown with a dotted line and is consistent with previous estimates (Wilson et al. 2008; Gonzalez et al. 2009; Rex et al. 2009).

2. Data and source catalog

The PACS and SPIRE observations of the Bullet cluster were reduced using the *Herschel* Interactive Processing Environment (HIPE). Small deviations from the standard pipeline are discussed in Egami et al. (2010).

2.1. Source selection

PACS and SPIRE data provide unprecedented sensitivities at FIR/submm wavelengths. Nonetheless, the precise identification of IR galaxies based solely on *Herschel* maps is complicated due to relatively large beam sizes leading to confusion noise in the SPIRE bands. We have therefore constructed an initial catalog with the positions of IR sources in the region based on secure (> 10-σ) detections in the higher resolution *Spitzer* MIPS 24 μm map of the field. A 10-σ 24 μm threshold corresponds to the 1-σ error in the PACS 100 μm map, our deepest *Herschel* map of the field. We select the positions for our photometry from this MIPS catalog in an effort to minimize the effect of Eddington bias which artificially boosts the flux of sources selected from confused submillimeter maps because of the steep underlying number counts. A proper statistical treatment of this effect will be presented in the more comprehensive analysis of this field in preparation.

In order to identify a subset of these initial sources which lie behind the Bullet cluster, we have compiled all of the spectroscopic redshift information for galaxies in the field obtained thus far. A description of these redshift catalogs and our method of association with the MIPS positions is given in Rawle et al. (2010). A histogram of the redshifts reveals a large group of Bullet cluster members at $z \sim 0.3$, as well as a smaller cluster of galaxies located just beyond at $z \sim 0.35$ (Rawle et al. 2010). We have therefore chosen a lower limit of $z \geq 0.40$ to select background field galaxies. With these criteria we assemble a sub-catalog of 50 MIPS-selected galaxies which are spectroscopically confirmed to be located behind the Bullet cluster. In many cases one SPIRE beam contains more than one MIPS galaxy. In these instances we are sometimes able to use the PACS resolution to identify the dominant source of the SPIRE emission. If this is not possible we exclude the source from our present anal-

ysis. Finally, we constrain our work to sources with > 3-σ detections in at least two *Herschel* bands. We are thereby left with a sample of 15 significant background galaxies with spectroscopic redshifts.

We also present the analysis of 4 additional galaxies selected because of photometric redshift (photo-z) estimates suggesting they are at $z_{phot} > 1.5$, and which are detected in LABOCA 870 μm (Johansson et al. 2010) and AzTEC 1.1 mm maps of the field (Wilson et al. 2008). We have calculated photo-z's for these sources using two methods: one based on IRAC colors (Pérez-González et al. 2005) and the other on the FIR–mm colors (Hughes et al. 2002; Aretxaga et al. 2003). When the two estimates disagree we have chosen the value which yields the lowest χ^2 fit to our SED templates. Including these galaxies in our analysis allows us to take advantage of the substantial correlation between SPIRE maps and longer wavelength submm/mm maps of the field. These results demonstrate the strength of combining such data sets to identify a potentially higher redshift galaxy population. The positions of our selections, along with corresponding MIPS and *Herschel* photometry can be found in table 1 (included in the online supplementary material).

2.2. Photometry

Herschel photometry for these galaxies is measured by simultaneously fitting the PSF at the positions of all of the 10-σ MIPS sources identified in our original catalog using routines included in the IRAF package DAOPHOT. To ensure the maps are aligned to the same astrometry small offsets are applied to the PACS data based on the results of stacking the 100 μm map on the MIPS positions and to the SPIRE data based on the results of stacking the 250 μm map on the MIPS positions. The 500 μm map is also corrected for contamination from the Sunyaev-Zel'dovich effect based on fits to the data presented in Zemcov et al. (2010) before performing photometry.

In cases where multiple MIPS galaxies fall within half the beam size at the corresponding waveband, we approximate the position of the group by the average of the counterparts weighted by their 24 μm signal-to-noise. We then take an iterative approach; fitting at the positions of the brightest sources first,
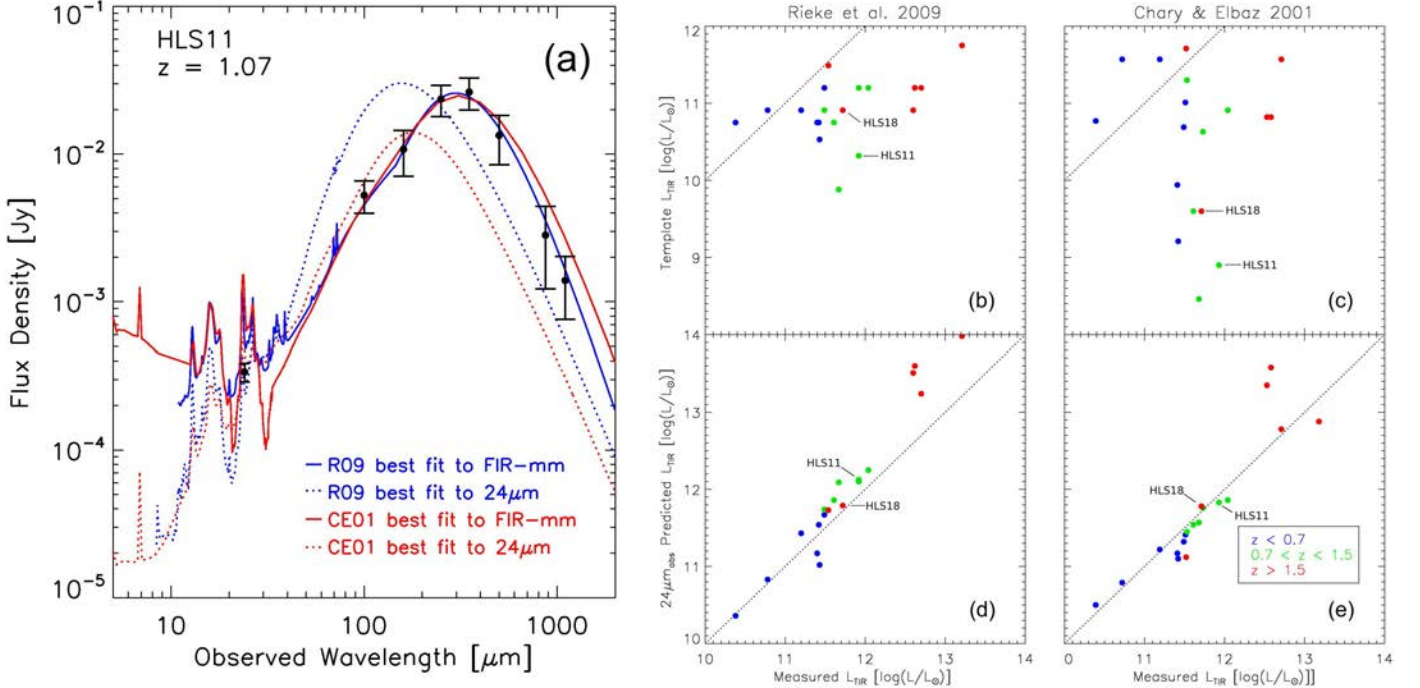
Fig. 2. *Left panel (a)*: SED template fits to HLS11, a redshift $z \sim 1$ LIRG. The data points have been de-magnified by a factor of 1.4 based on our lensing models of the foreground cluster. Although both the R09 and the CE01 templates predict the IR luminosity based on observed $24\,\mu$m emission to within a factor of 2, the $24\,\mu$m-predicted SEDs do not provide reasonable fits to the FIR–mm data. *Right top panels (b & c)*: The IR luminosity of the best-fit template as it corresponds to the local population is plotted as a function of the actual IR luminosity of each galaxy. The SEDs of our sample are better fit by templates corresponding to systematically lower luminosity local galaxies. *Right bottom panels (d & e)*: The $24\,\mu$m-predicted IR luminosity is plotted as a function of the actual IR luminosity of each galaxy. Both template families predict reasonable values for the luminosities of the galaxies in our sample, except in the cases of the ULIRGS/Hyper-LIRGS at $z > 1.5$. Note that HLS11 & HLS18 (Fig. 1) fall on the trend line even though their SED shapes show significant deviation in (b) & (c).

removing them from the map, fitting at the positions of the next tier, and so on until we have reached the 3-σ noise level of the observation. This method is similar to that outlined in Pérez-González et al. (2010), although we force the algorithm to fit the PSF at the MIPS positions rather than allowing for any re-centering.

Our analysis includes LABOCA $870\,\mu$m and AzTEC 1.1 mm photometry for our sources when it is of > 3-σ significance. Four of our objects have LABOCA counterparts within 8″ listed in the photometric catalog from Johansson et al. (2010). In these cases we use the deboosted flux given in the catalog for our analysis. In order to obtain photometry for the remaining sources, we measure the flux in an aperture of 40″ at the MIPS position in order to get the total flux from the beam. This method is not the same as that used in Johansson et al. (2010), although it gives consistent results for the 17 sources presented therein. In the case of the four sources chosen, in part, due to bright long-wavelength emission, we identify clear associations between the MIPS source and a significant, individual AzTEC source. In these cases we use the deboosted flux from the AzTEC catalog. For the other sources the AzTEC fluxes are measured at the MIPS positions from a PSF-convolved map. In the instances where there is a counterpart (within 8″) in the AzTEC catalog, the difference between the flux at the MIPS position and the deboosted point-source flux is < 10%.

3. Results

Figure 1 shows the most highly magnified galaxy in our sample, first reported as a strongly lensed IRAC source (Bradač et al. 2006; Gonzalez et al. 2009) and independently found to be the brightest submm/mm source in the field (Wilson et al. 2008; Rex et al. 2009; Johansson et al. 2010). Multiple images of the galaxy are indicated with white circles. The right panel shows our SED fit to the sum of the fluxes from the brightest of the two images. SPIRE data indicate a $250\,\mu$m flux density which is 30% lower than that measured in the BLAST data (Rex et al. 2009), although the measurements are consistent within the uncertainties. The *Spitzer* InfraRed Spectrograph (IRS) spectrum of this source confirms that it is at redshift $z = 2.79$ (Gonzalez et al. 2010), consistent with published photo-z estimates similar to the ones used for the four sources in our sample which lack spectroscopic redshift information. At that redshift, our model indicates a magnification of ~ 50 due to gravitational lensing by the foreground cluster. This value is lower than other estimates presented in the literature (e.g. Gonzalez et al. (2010) suggest a magnification of ~ 100). We note that this value should be treated as a lower limit since there is likely to be additional local lensing from nearby objects. We derive an observed IR luminosity of 2.8×10^{13} L$_\odot$ based on the template SED fitting (see below for a detailed discussion of this SED fitting procedure). Adopting our estimated lower limit for the magnification of the source indicates an intrinsic IR luminosity of $\lesssim 5 \times 10^{11}$ L$_\odot$ which is consistent with calculations previously reported in the literature (Wilson et al. 2008; Gonzalez et al. 2009; Rex et al.

2009; Gonzalez et al. 2010), apart from the assumed magnification factor. The detection of such an intrisically faint galaxy is not possible without gravitational lensing, clearly demonstrating the power and promise of our strategy.

3.1. SED properties

The galaxies in our sample span a redshift range of $0.40 < z < 3.24$. Knowing their redshifts, we can derive their apparent IR luminosities. We use the lensing models described in Paraficz et al. (in prep.) to correct for the magnification of each source due to gravitational lensing by the foreground cluster and calculate the galaxies' intrinsic properties. In our discussion of IR properties, we adopt nomenclature similar to that in Rieke et al. (2009), defining the total IR luminosity (L_{TIR}) as the luminosity in the rest-frame wavelength range $\lambda = 5$–$1000\,\mu m$. The redshifts, magnifications, and de-magnified IR luminosities of each source are listed in table 2. We assume a ΛCDM cosmology with $\Omega_m = 0.3$, $\Omega_\Lambda = 0.7$, and $H_0 = 70\,km\,s^{-1}Mpc^{-1}$ for our calculations.

We use a χ^2 minimization routine to fit the SED templates presented in Rieke et al. (2009) (R09), as well as those presented in Chary & Elbaz (2001) (CE01). These templates are based on data from local galaxies and each is designated by a luminosity class corresponding to the total infrared luminosities of the local (U)LIRGS for which it provides the best fit. The left panel of Fig. 2 shows an example of the template fits to a galaxy in our sample. The solid lines show the best-fit R09 template (in blue) and CE01 template (in red) to the FIR–mm data, excluding the $24\,\mu m$ point. The dotted lines show the respective fits to only the observed $24\,\mu m$ point. The SED fits to the remaining galaxies in our sample are shown in Figs. 3 and 4 (included in the online supplementary material).

In general we find that the templates provide good fits to the FIR–mm data in our galaxy sample and that the IR luminosities derived using the best-fit templates from both R09 and CE01 agree within a 1-σ spread of 15%. We also find that the galaxies in our sample are best fit by templates with systematically lower luminosity classes. The top right panels (b & c) of Fig. 2 illustrate this trend. The luminosity class of the best-fit template to each galaxy is plotted as a function of the actual luminosity for the R09 templates in (b) and the CE01 templates in (c). Although we find a large scatter in the luminosity classes of best-fit SEDs, both template families show the same general trend. This is because the SEDs of our galaxies peak at longer wavelengths than local galaxies of comparable luminosities. Therefore their spectral shapes more closely resemble those of lower luminosity (U)LIRGS in the local universe. The result supports evidence that high-redshift submm galaxies are cooler than local galaxies with similar IR luminosities, suggesting the star formation within them is occurring on more extended physical scales (e.g. Chapman et al. 2004).

The discrepancy between the FIR SED shapes of our sources and those of local counterparts with similar luminosities implies that a blind application of the local template SED models might not accurately predict the L_{TIR} and hence the SFRs of higher redshift submm galaxies. However, other studies based on *Herschel* data show that the L_{TIR} predicted by observed $24\,\mu m$ emission is in good agreement with that measured from the FIR data for galaxies at $z < 1.5$ (Elbaz et al. 2010). The bottom right panels of Fig. 2 confirm this trend. The IR luminosity derived from $24\,\mu m$ is plotted as a function of the actual IR luminosity for the R09 templates in (d) and the CE01 templates in (e). Although the R09 fits show a slightly higher deviation, both template families

predict reasonable values for the luminosities of the galaxies in our sample, except in the cases of the ULIRGS/Hyper-LIRGS at $z > 1.5$. The left panel of Fig. 2 shows a closer inspection of the SED fits, revealing that although the predicted IR luminosities are consistant with the measured values, the SED templates selected based solely on observed $24\,\mu m$ emission typically peak at shorter wavelengths, and do not provide good fits to the FIR–mm data.

4. Conclusion

We have presented the first *Herschel* analysis of galaxies located behind the Bullet cluster. We find that their colors are best fit using templates based on local galaxies with systematically lower IR luminosities. This suggests that our sources are not like local ULIRGS in which vigorous star formation is contained in a compact highly dust-obscured region. Instead, they appear to be scaled up versions of lower luminosity local galaxies with star formation occurring on larger physical scales. A more comprehensive analysis of the field in preparation will combine our full catalog of sources with LABOCA and AzTEC data to compile a larger sample of these galaxies. By studying their relationship to local star-forming galaxies we can better understand the processes that govern their evolution.

Table 2. Source properties.

ID	z	Mag	R09 L_{TIR} [$L_\odot$]
HLS01	0.61	1.1	2.6e+11
HLS02	[a] $\mathbf{2.7^{+.1}_{-.1}}$, $4.1^{+.7}_{-.6}$	1.00	4.0e+12
HLS03	0.72	1.0	3.1e+11
HLS04	0.82	1.0	4.1e+11
HLS05	[a] $\mathbf{1.6^{+.1}_{-.1}}$, $\mathbf{1.6^{+.4}_{-.1}}$	1.16	1.6e+13
HLS06	[a] $\mathbf{2.8^{+.1}_{-.1}}$, $\mathbf{1.8^{+.5}_{-.4}}$	1.11	5.0e+12
HLS07	0.66	1.1	1.6e+11
HLS08	0.43	1.2	2.4e+10
HLS08	0.82	1.1	8.3e+11
HLS10	0.60	1.1	3.1e+11
HLS11	1.07	1.4	8.3e+11
HLS12	3.24	11.3	3.5e+11
HLS13	[a] $\mathbf{2.9^{+.1}_{-.1}}$, $3.1^{+.7}_{-.3}$	1.23	4.2e+12
HLS14	0.57	1.1	6.0e+10
HLS15	1.17	1.1	4.7e+11
HLS16	0.45	1.4	2.5e+11
HLS17	0.40	1.1	2.7e+11
HLS18	2.79	>54[b]	5.2e+11
HLS19	0.71	1.1	1.1e+12

[a] IRAC photo-z, FIR-mm photo-z. Adopted value in bold.
[b] Lower limit due to unquantified local lensing by nearby objects.

References

Aretxaga, I., Hughes, D. H., Chapin, E. L., et al. 2003, MNRAS, 342, 759
Bradač, M., Clowe, D., Gonzalez, A. H., et al. 2006, ApJ, 652, 937
Chapman, S. C., Smail, I., Windhorst, R., Muxlow, T., & Ivison, R. J. 2004, ApJ, 611, 732
Chary, R. & Elbaz, D. 2001, ApJ, 556, 562

Egami, E. et al. 2010, A&A, this volume
Elbaz, D. et al. 2010, A&A, this volume
Gonzalez, A. H., Clowe, D., Bradač, M., et al. 2009, ApJ, 691, 525
Gonzalez, A. H., Papovich, D., Bradač, M., & Jones, C. 2010, ApJ, submitted
Griffin, M. et al. 2010, A&A, this volume
Hughes, D. H., Aretxaga, I., Chapin, E. L., et al. 2002, MNRAS, 335, 871
Johansson, D., Horellou, C., Sommer, M. W., et al. 2010, arXiv:1003.0827
Kennicutt, Jr., R. C. 1998, ApJ, 498, 541
Pérez-González, P. et al. 2010, A&A, this volume
Pérez-González, P. G., Rieke, G. H., Egami, E., et al. 2005, ApJ, 630, 82
Pilbratt, G. et al. 2010, A&A, this volume
Poglitsch, A. et al. 2010, A&A, this volume
Rawle, T. et al. 2010, A&A, this volume
Rex, M., Ade, P. A. R., Aretxaga, I., et al. 2009, ApJ, 703, 348
Rieke, G. H., Alonso-Herrero, A., Weiner, B. J., et al. 2009, ApJ, 692, 556
Wilson, G. W., Hughes, D. H., Aretxaga, I., et al. 2008, MNRAS, 390, 1061
Zemcov, M. et al. 2010, A&A, this volume

[1] Steward Observatory, University of Arizona, 933 N. Cherry Ave, Tucson, AZ 85721, USA; e-mail: mrex@as.arizona.edu
[2] Departamento de Astrofísica, Facultad de CC. Físicas, Universidad Complutense de Madrid, E-28040 Madrid, Spain
[3] California Institute of Technology, Pasadena, CA 91125, USA
[4] Jet Propulsion Laboratory, Pasadena, CA 91109, USA
[5] Instituto Nacional de Astrofísica Óptica y Electrónica (INAOE), Luis Enrique Erro No.1, Tonantzintla, Puebla, C.P. 72840, Mexico
[6] Department of Astronomy, University of Florida, Gainesville, FL 32611-2055, USA
[7] NASA Herschel Science Center, California Institute of Technology, MS 100-22, Pasadena, CA 91125, USA
[8] Onsala Space Observatory, Chalmers University of Technology, SE-439 92 Onsala, Sweden
[9] Laboratoire d'Astrophysique de Marseille, CNRS - Université Aix-Marseille, 38 rue Frédéric Joliot-Curie, 13388 Marseille Cedex 13, France
[10] Institute for Computational Cosmology, Department of Physics, Durham University, South Road, Durham DH1 3LE, UK
[11] Herschel Science Centre, ESAC, ESA, PO Box 78, Villanueva de la Cañada, 28691 Madrid, Spain
[12] Laboratoire d'Astrophysique de Toulouse-Tarbes, Université de Toulouse, CNRS, 14 Av. Edouard Belin, 31400 Toulouse, France
[13] Observatoire de Paris, LERMA, 61 Av. de l'Observatoire, 75014 Paris, France
[14] Geneva Observatory, University of Geneva, 51, Ch. des Maillettes, CH-1290 Versoix, Switzerland
[15] UK Astronomy Technology Centre, Science and Technology Facilities Council, Royal Observatory, Blackford Hill, Edinburgh EH9 3HJ, UK
[16] Institute for Astronomy, University of Edinburgh, Blackford Hill, Edinburgh EH9 3HJ, UK
[17] Max-Planck-Institut für extraterrestrische Physik, Postfach 1312, 85741 Garching, Germany
[18] Institut d'Astrophysique de Paris, CNRS and Université Pierre et Marie Curie, 98bis Boulevard Arago, F-75014 Paris, France
[19] Department of Astronomy, University of Padova, Vicolo dell'Osservatorio 3, I-35122 Padova, Italy
[20] School of Physics and Astronomy, University of Birmingham, Edgbaston, Birmingham, B15 2TT, UK
[21] Sterrewacht Leiden, Leiden University, PO Box 9513, 2300 RA Leiden, the Netherlands
[22] Center for Astrophysics and Space Astronomy, University of Colorado, Boulder, CO 80309, USA
[23] Nobeyama Radio Observatory, National Astronomical Observatory of Japan, Minamimaki, Minamisaku, Nagano 384-1305 Japan
[24] Institute of Astronomy, University of Tokyo, 2-21-1 Osawa, Mitaka, Tokyo 181-0015, Japan
[25] Research Center for the Early Universe, School of Science, University of Tokyo,7-3-1 Hongo, Bunkyo, Tokyo 113-0033, Japan
[26] Department of Physics, Illinois Wesleyan University,Bloomington, IL 61702-2900, USA
[27] Department of Physics & Astronomy, University of Pennsylvania, 209 South 33rd Street, Philadelphia, PA 19104, USA
[28] Department of Astronomy, University of Massachusetts, 710 North Pleasant Street, Amherst, MA 01003, USA

Table 1. Flux densities measured from the MIPS and *Herschel* maps. The $500\,\mu$m map was corrected for SZ contamination before extracting the photometry. These measurements have not been corrected for the amplification due to gravitational lensing.

ID	RA [deg]	Dec [deg]	Flux$_{24}$ [mJy]	Flux$_{100}$ [mJy]	Flux$_{160}$ [mJy]	Flux$_{250}$ [mJy]	Flux$_{350}$ [mJy]	Flux$_{500}$ [mJy]
HLS01	104.72828	-55.88917	0.40± 0.01	...	...	21.1± 2.5	10.0± 3.5	< 7.8^b
HLS02	104.46419	-56.02209	0.15± 0.01	...	...	10.1± 2.4	16.2± 3.5	14.4± 4.0
HLS03	104.48783	-56.03070	0.39± 0.02	...	...	9.0± 2.4	9.5± 3.4	< 7.8^b
HLS04	104.45727	-55.91533	0.39± 0.01	...	...	18.6± 2.8	13.2± 3.6	< 7.8^b
HLS05	104.60260	-55.92013	0.71± 0.02	75.4± 1.3	164.4± 5.1	168.9± 6.2	120.0± 4.1	58.4± 4.4
HLS06	104.64300	-55.90990	0.40± 0.01	9.9± 1.2	28.4± 2.4	44.6± 2.8	39.0± 3.5	25.2± 4.0
HLS07	104.60545	-55.89051	0.29± 0.01	7.0± 1.3	7.8± 2.1	8.2± 2.8	< 8.4^b	< 7.8^b
HLS08	104.63628	-55.98351	0.135± 0.003	2.7± 1.1	4.6± 2.1	< 6.0^b	< 8.4^b	< 7.8^b
HLS09	104.55591	-55.87279	0.65± 0.02	...	...	23.2± 2.6	12.9± 3.5	< 7.8^b
HLS10	104.54350	-55.98005	0.53± 0.02	16.7± 1.4	22.6± 2.1	13.9± 2.4	< 8.4^b	< 7.8^b
HLS11	104.56008	-55.95848	0.47± 0.01	7.4± 1.1	15.1± 2.1	33.1± 2.7	36.9± 3.5	18.8± 4.1
HLS12	104.62997	-55.94386	0.046± 0.003	< 2.4^b	4.3± 2.1	7.8± 2.5	11.4± 3.4	< 7.8^b
HLS13	104.60567	-55.94490	0.28± 0.01	2.9± 1.1	5.5± 2.0	10.1± 2.5	19.6± 3.5	< 7.8^b
HLS14	104.64689	-55.88658	0.136± 0.004	3.0± 1.2	4.4± 2.1	< 6.0^b	< 8.4^b	< 7.8^b
HLS15	104.73730	-55.88516	0.16± 0.02	...	...	11.1± 2.7	15.3± 3.8	11.7± 3.7
HLS16	104.58575	-55.93920	0.83± 0.02	25.3± 1.3	51.3± 2.5	47.7± 2.6	24.0± 3.6	10.2± 3.7
HLS17	104.64463	-56.00850	0.71± 0.02	24.7± 1.2	56.5± 3.4	49.2± 3.4	35.5± 3.7	17.9± 3.7
HLS18$_A$^{a}	104.65471	-55.95193	0.49± 0.01	7.0± 1.2	24.5± 2.1	65.3± 2.8	98.6± 3.9	101.4± 4.0
HLS18$_B$^{a}	104.65861	-55.95057	0.36± 0.01	3.8± 1.1	14.0± 2.5	< 6.0^b	< 8.4^b	< 7.8^b
HLS19	104.59877	-55.87833	1.10± 0.03	...	...	40.9± 2.9	21.6± 4.0	9.4± 3.7

[a] Multiple images of the highly lensed galaxy (Gonzalez et al. 2009).
[b] Upper limits correspond to statistical 3-σ noise levels of each map.
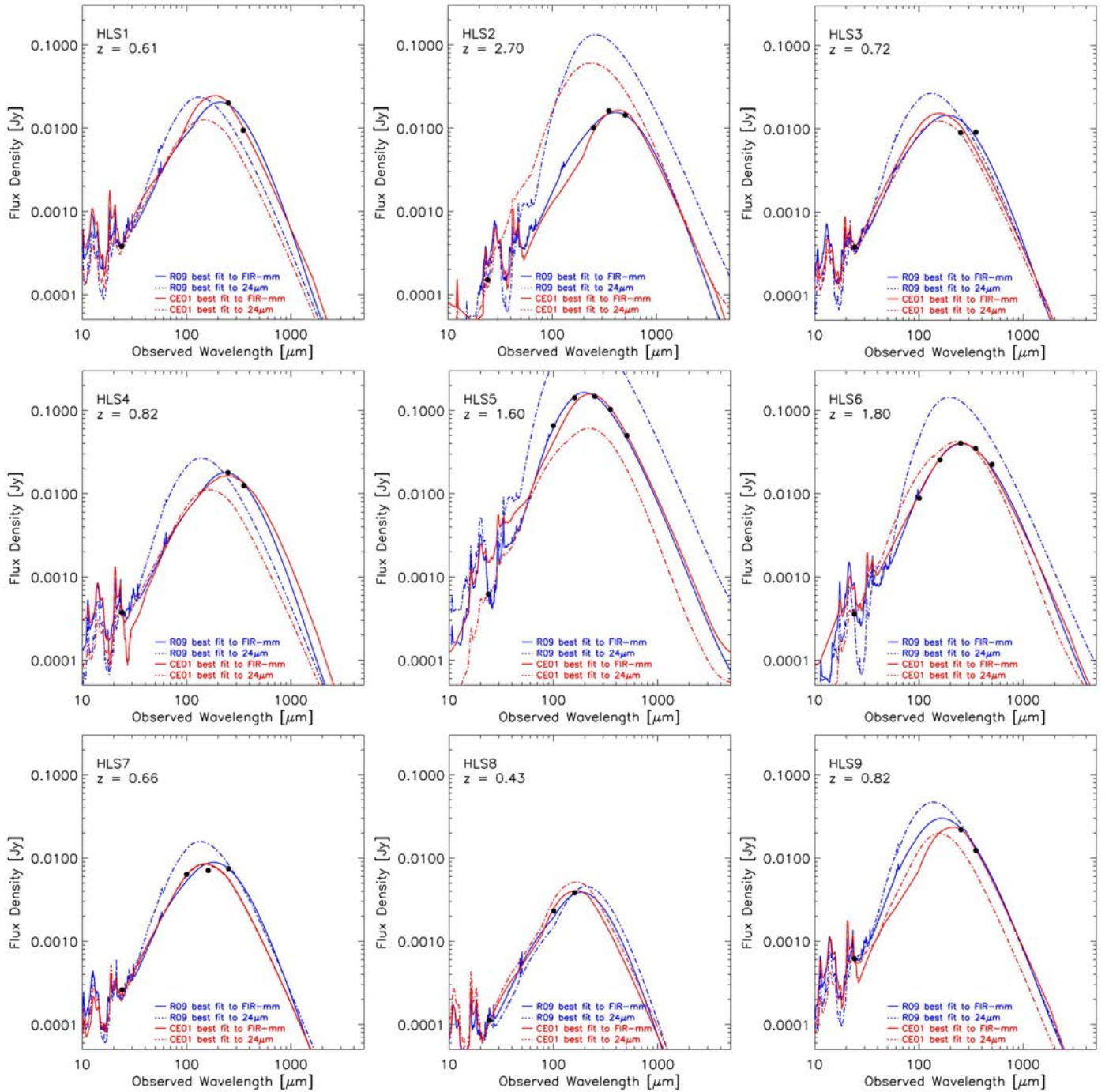
Fig. 3. SED template fits to HLS1–HLS9. The data points have been de-magnified according to our lensing models of the foreground cluster. These magnification factors can be found in table 2. The solid lines show the best-fit R09 template (in blue) and CE01 template (in red) to the FIR–mm data, excluding the 24 μm point. LABOCA 870 μm and AzTEC 1.1 mm data are used to constrain these fits when the detection is of > 3-σ significance. However, only the MIPS and *Herschel* data are shown in the figure. The dotted lines show the respective fits based solely on the observed 24 μm point. Although both the R09 and the CE01 templates generally predict reasonable values for the IR luminosity based on observed 24 μm emission, the 24 μm-predicted SEDs typically do not provide reasonable fits to the FIR–mm data.
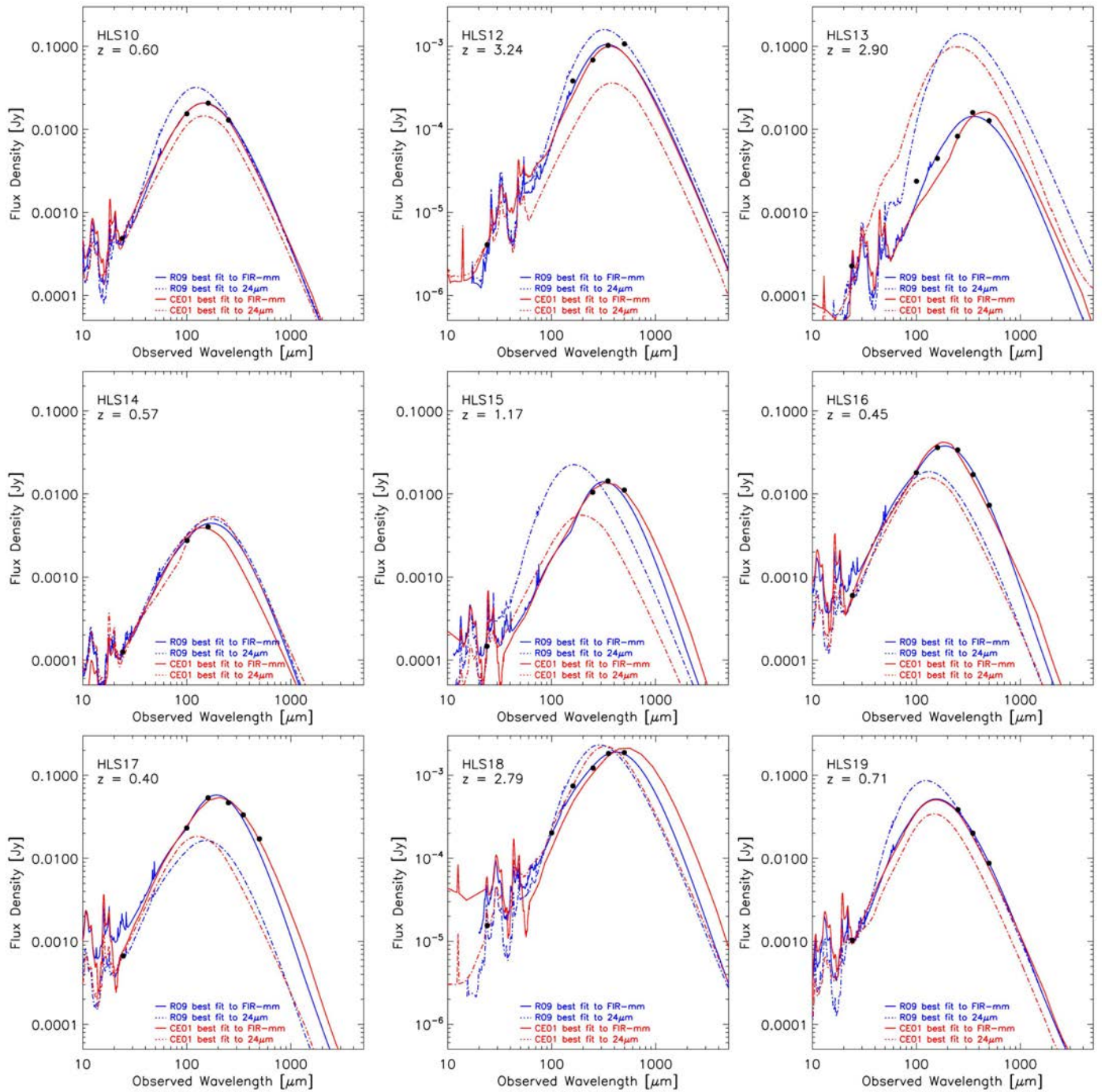
Fig. 4. SED template fits to HLS10–HLS19. The data points have been de-magnified according to our lensing models of the foreground cluster. These magnification factors can be found in table 2. The solid lines show the best-fit R09 template (in blue) and CE01 template (in red) to the FIR–mm data, excluding the $24\,\mu$m point. LABOCA $870\,\mu$m and AzTEC 1.1 mm data are used to constrain these fits when the detection is of > 3-σ significance. However, only the MIPS and *Herschel* data are shown in the figure. The dotted lines show the respective fits based solely on the observed $24\,\mu$m point. Although both the R09 and the CE01 templates generally predict reasonable values for the IR luminosity based on observed $24\,\mu$m emission, the $24\,\mu$m-predicted SEDs typically do not provide reasonable fits to the FIR–mm data.